Tight Bounds and the Role of Optical Loss in Polariton-Mediated Near-Field Heat Transfer

Mariano Pascale and Georgia T. Papadakis*

ICFO-Institut de Ciencies Fotoniques, The Barcelona Institute of Science and Technology, Castelldefels, Barcelona 08860, Spain

(Received 22 June 2022; revised 8 February 2023; accepted 9 February 2023; published 3 March 2023; corrected 21 June 2023)

We introduce an analytical framework for near-field radiative heat transfer in bulk plasmonic and polar media. Considering material dispersion, we derive a closed-form expression for the radiative thermal conductance, which disentangles the role of optical loss from other material dispersion characteristics, such as the spectral width of the Reststrahlen band in polar dielectrics, as well as from the temperature. We provide a universal condition for maximizing heat transfer that defines the optimal interplay between a material's optical loss and polariton resonance frequency, based on which we introduce tight bounds to near-field heat transfer. With this formalism, one can quantitatively evaluate all polaritonic materials in terms of their performance as near-field thermal emitters.

DOI: 10.1103/PhysRevApplied.19.034013

I. INTRODUCTION

Radiative heat transfer between bodies separated by nanometric vacuum gaps can surpass the blackbody limit by several orders of magnitude [1–7]. This creates opportunities in a wide range of applications where thermal control is critical. Examples include high-efficiency energy conversion with thermophotovoltaic systems [8–13], contactless cooling [14,15], thermal lithography [16–19], thermally assisted magnetic recording [20–22], and thermal logic circuitry [23–26].

Accessing the thermal near field, where the separation distance between objects is smaller than the relevant thermal wavelength, typically of the order of a few microns, yields ultrahigh radiative heat transfer (of the order of tens of W/cm^2 [2,5,27–30]). In this range, radiative heat is optimally transferred by evanescent modes, such as surface plasmon polaritons (SPPs) and surface phonon polaritons (SPhPs) [29,31], that tunnel across a nanometric vacuum gap. SPPs are resonantly excited on a plasmonic metal surface [32], e.g., Au or Ag, at frequencies ranging from near-infrared (IR) to ultraviolet [33]. On the other hand, SPhPs are surface resonant modes occurring on polar dielectrics and semiconductors, e.g., hexagonal BN, SiC, or GaAs, at frequencies ranging from mid-IR to < 10 THz [31].

Near-field radiative heat transfer (NFRHT) is rigorously described within the framework of fluctuational electrodynamics (FE) [1,2]. Computing the total NFRHT between bodies requires carrying out a spectral as well as a spatial integration of the exchanged thermal radiation over the entire frequency spectrum and for all relevant wave numbers, respectively. This integration remains challenging in practice even in the simplest case of NFRHT between semi-infinite planar layers, for which numerical approaches are usually employed [34,35]. Most importantly, although optical loss and thermal fluctuations are fundamentally connected via the fluctuation-dissipation theorem [1], the dependence of NFRHT on the optical loss of materials remains unidentified.

Upper bounds to the thermal emission spectrum per frequency [termed $\Phi(\omega)$; see Eq. (2) below] have recently been analytically estimated [16,36–39]. Furthermore, upper bounds to the integrated radiative thermal conductance [Eq. (1) below] have been reported in Refs. [36,38,40]. In Refs. [41,42], analytical solutions to the total integrated heat transfer for polaritonic media were reported. Nonetheless, critical material parameters such as the polariton resonance frequency, the optical loss, as well as other dispersion characteristics, have remained mathematically intertwined. This prohibits a deep physical understanding of the role of each in NFRHT.

In this work, we provide a general and fully analytical framework for NFRHT mediated by surface polaritons in planar bulk systems. Thus, we identify the explicit dependence of NFRHT on material loss, and thereby derive a universal optimal loss condition that maximizes NFRHT. With respect to previous contributions [36,38], by taking into account actual material dispersion, we introduce a temperature-independent tight upper bound to NFRHT. Furthermore, we carry out a quantitative classification of all polaritonic media in terms of NFRHT performance. Although the presented analytical framework models materials characterized by a single

*Georgia.Papadakis@icfo.eu

polariton resonance, we also show a semianalytical extension able to describe multiple polaritonic resonances.

II. RESULTS AND DISCUSSION

A. Emission spectrum

We describe NFRHT at mean temperature T by evaluating the radiative thermal conductance per unit area [43]:

$$h = \int_0^\infty \left[\frac{\partial}{\partial T}\theta(\omega, T)\right]\Phi(\omega)d\omega. \tag{1}$$

Here $\theta(\omega, T) = \hbar\omega/[\exp(\hbar\omega/k_B T) - 1]$ is the mean energy per photon and $\Phi(\omega)$ is the thermal emission spectrum, expressed in m^{-2}. We consider a vacuum gap of size d that separates two planar semi-infinite bodies exchanging heat. The bodies are made of nonmagnetic, isotropic, homogeneous material with relative dielectric permittivity $\varepsilon(\omega)$ and susceptibility $\chi(\omega) = \varepsilon(\omega) - 1$. From fluctuational electrodynamics [1,2,44,45], $\Phi(\omega)$ is given by

$$\Phi(\omega) = \frac{1}{4\pi^2}\int_0^\infty [\xi_p(\omega, \beta) + \xi_s(\omega, \beta)]\beta\, d\beta, \tag{2}$$

where $\xi_{p,s}(\omega, \beta)$ is the probability for a photon at frequency ω and in-plane wave number β to tunnel across the gap. The subscripts p and s denote polarization, corresponding to TM (transverse magnetic) and TE (transverse electric), respectively.

For gap sizes smaller than the thermal wavelength, $\lambda_T = b_{\mathrm{Wien}}/T$, where $b_{\mathrm{Wien}} = 2989\ \mu\mathrm{m\,K}$ [46], thermally excited SPPs and SPhPs dominate NFRHT in plasmonic and polar materials, respectively. Since these can only be excited in p-polarization [32], the emission spectrum Φ can be approximated as the contribution from p-polarization alone. At sufficiently small vacuum gaps, the dispersion of surface polaritons approaches the quasistatic limit, for which $\beta \gg k_0$ [16], where $k_0 = \omega/c$ is the free-space wave number. In this limit, as shown in Eq. (A2) of Appendix A, the maximum in-plane wave number $\beta_{\max}$ that satisfies the perfect photon tunneling condition, i.e., $\xi_p = 1$, occurs near the surface polariton resonance frequency Ω at which $\mathrm{Re}\{r_p\} = 0$, where $r_p(\omega) = \chi(\omega)/(\chi(\omega) + 2)$ is the Fresnel coefficient in the quasistatic regime, or

$$\mathrm{Re}\left\{\frac{2}{\chi(\Omega)}\right\} = -1. \tag{3}$$

For low-loss materials, i.e., for $\mathrm{Im}\{\chi(\Omega)\} \ll 1$, Eq. (3) reduces to the more common expression $\mathrm{Re}\{\chi(\Omega)\} = -2$ [32].

To obtain the emission spectrum, we carry out the integration of Eq. (2), over all available wave numbers β. Upon assuming that $\beta \gg k_0$, this integration yields

$$\Phi(\omega) = \frac{1}{8\pi^2 d^2}\frac{\mathrm{Im}\{r_p(\omega)\}}{\mathrm{Re}\{r_p(\omega)\}}\mathrm{Im}\{\mathrm{Li}_2[r_p^2(\omega)]\}, \tag{4}$$

where Li_2 is the dilogarithm or Spence's function [47], given in Eq. (A7) of Appendix A. This expression agrees with Rousseau *et al.* [41]. Its derivation, along with the more general expression for heat exchange between dissimilar materials, can be found in Appendix A, where we also showcase the validity of Eq. (4). Equation (4) directly computes the thermal emission spectrum, once provided the Fresnel coefficients, and is valid for *any* material's frequency dispersion. In the low-loss limit, the emission spectrum is maximum at $\omega = \Omega$, where Eq. (4) reduces to the result of Miller *et al.* [37], as shown in Appendix A, where we discuss an approach to quantitatively distinguish the low-loss regime from the high-loss regime in NFRHT [Eq. (B10) in Appendix B].

The dielectric function of most plasmonic and polar materials can be respectively described by single Drude and Lorentz oscillators:

$$\varepsilon(\omega) = \begin{cases} \varepsilon_{\mathrm{plasm}} = \varepsilon_\infty\left[1 - \dfrac{\omega_p^2}{\omega(\omega + i\gamma)}\right], & \text{(5a)} \\ \varepsilon_{\mathrm{polar}} = \varepsilon_\infty\left[1 + \dfrac{\omega_{\mathrm{LO}}^2 - \omega_{\mathrm{TO}}^2}{\omega_{\mathrm{TO}}^2 - \omega^2 - i\omega\gamma}\right]. & \text{(5b)} \end{cases}$$

Here ε_∞ is the high-frequency relative permittivity and γ is the optical loss [48,49]. For plasmonic metals, ω_p is the plasma frequency, near which the SPP mode occurs. For polar materials, ω_{TO} and ω_{LO} are the transverse and longitudinal optical phonon frequencies, respectively [31]. The spectral range $[\omega_{\mathrm{TO}}, \omega_{\mathrm{LO}}]$ defines the *Reststrahlen* band [50], within which the SPhP mode occurs.

The resonance frequency Ω is found by solving Eq. (3). Since Ω does not vary significantly as γ increases (see Appendix C), we evaluate it for $\gamma \to 0$ as

$$\Omega = \begin{cases} \Omega_{\mathrm{plasm}} = \sqrt{\dfrac{\varepsilon_\infty}{\varepsilon_\infty + 1}}\omega_p, & \text{(6a)} \\ \Omega_{\mathrm{polar}} = \sqrt{\dfrac{\varepsilon_\infty\omega_{\mathrm{LO}}^2 + \omega_{\mathrm{TO}}^2}{1 + \varepsilon_\infty}}. & \text{(6b)} \end{cases}$$

Henceforth, we assume that Ω_{plasm} and Ω_{polar} are γ independent.

As an example, in Fig. 1 we plot $\Phi(\omega)$ normalized with d^2 for silicon carbide (SiC), a widely used polar dielectric in the NFRHT literature [29,43,51]. We consider a representative Lorentz model for its permittivity, with $\varepsilon_\infty = 6.7$, $\omega_{\mathrm{TO}} = 1.49 \times 10^{14}$ rad/s, $\omega_{\mathrm{LO}} = 1.83 \times 10^{14}$ rad/s, $\gamma = 8.97 \times 10^{11}$ rad/s [52]. The exact emission spectrum

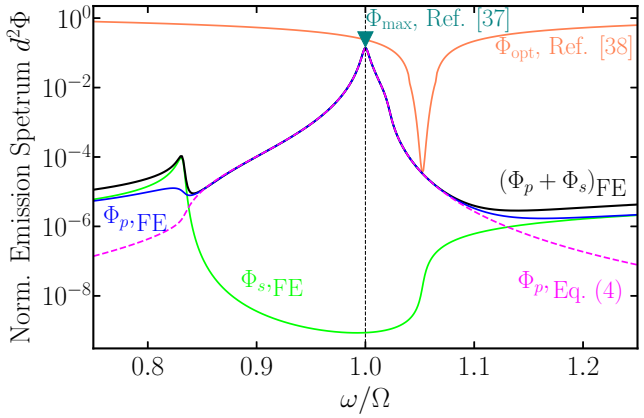

FIG. 1. Thermal emission spectrum Φ normalized by d^{-2} as a function of frequency, in the neighborhood of the SPhP resonance Ω for two bulk planar layers made of SiC exchanging thermal radiation in the near field. Here $\Phi_{p,\text{FE}}$, $\Phi_{s,\text{FE}}$, and $\Phi = (\Phi_p + \Phi_p)_{\text{FE}}$, shown with blue, green, and black curves, respectively, correspond to the p-polarization, s-polarization, and total spectrum as computed via fluctuational electrodynamics, whereas the analytical prediction in Eq. (4) as well as in Ref. [41] is shown with the magenta dashed line. We also show the spectral upper bound Φ_{opt} from Ref. [38] (orange curve) and the emission spectrum at the resonance frequency from Ref. [37] (teal triangle), given in Eq. (A10) of Appendix A.

for p-polarization ($\Phi_{p,\text{FE}}$), obtained via numerical integration with no approximations, is shown with the blue curve. Its s-polarization counterpart ($\Phi_{s,\text{FE}}$) as well as their sum, $\Phi = (\Phi_p + \Phi_p)_{\text{FE}}$, are shown with the green and black curves, respectively. As anticipated, the p-polarization component dominates the emission spectrum in almost the entire frequency range near Ω, and thus coincides with the total Φ. Importantly, the magenta dashed curve shows Φ_p obtained with the analytical solution in Eq. (4) and in Ref. [41]. This curve overlaps nearly perfectly with FE for frequencies near resonance. We also display an upper bound to the spectrum of NFRHT, Φ_{opt}, as derived by Venkataram *et al.* [38], obtained through singular value decomposition of the Maxwell Green tensor. This result accurately estimates the response of SiC only on resonance. Similarly, we show with a triangle-shaped marker the upper bound to NFRHT on resonance, derived by Miller *et al.* [37], and given in Eq. (A10) of Appendix A.

B. Optimal loss and upper bounds

In evaluating NFRHT performance, it is useful to introduce a material quality factor for the polaritonic resonance in plasmonic and polar media [31,53,54]:

$$Q = \left.\frac{\omega \frac{d\varepsilon}{d\omega}}{2\text{Im}\{\varepsilon\}}\right|_{\Omega} \approx \frac{\Omega}{\gamma}. \tag{7}$$

To obtain the radiative thermal conductance [Eq. (1)], we use contour integration in the complex frequency plane of Φ (see Appendices B and C), similar to Ref. [41]. Considering that the Planck distribution varies slowly with respect to $\Phi(\omega)$, we obtain

$$h = h_{\max}\Psi\left(\frac{Q}{B}\right)\Pi\left(\frac{\Omega}{T}\right). \tag{8}$$

The functions Π and Ψ are given by

$$\Pi\left(\frac{\Omega}{T}\right) = \frac{1}{k_B}\frac{\partial}{\partial T}\theta(\Omega, T) = \left[\frac{\frac{h}{2kB}\frac{\Omega}{T}}{\sinh\left(\frac{h}{2kB}\frac{\Omega}{T}\right)}\right]^2, \tag{9}$$

$$\Psi\left(\frac{Q}{B}\right) = \left.\frac{h}{h_{\max}}\right|_{T\gg\hbar\Omega/2k_B} = -\frac{\text{Li}_2[-(Q/B)^2]}{1.36(Q/B)}. \tag{10}$$

These functions are both bounded above by unity; hence, $h_{\max}$ in Eq. (8) defines the maximum thermal conductance that a polaritonic material can reach in a planar configuration, and is given by

$$h_{\max} = \frac{1.36k_B}{16\pi d^2}\frac{\Omega}{B}. \tag{11}$$

As can be seen, $h_{\max}$ is temperature and loss independent. Furthermore, it expresses the well-known $\propto d^{-2}$ dependence of NFRHT from the vacuum gap size [34,36,41,42]. It must be noted that this result is valid within a macroscopic description of thermal fluctuations. To properly estimate how NFRHT scales in the limit $d \to 0$, often referred to as the "extreme near field," one should consider effects relevant at microscopic scales, e.g., transport properties of the materials as well as the nonlocal electromagnetic response [55–58].

Parameter B is termed the *material residue* henceforth, and it is defined as $B = Q/\text{Im}\{r_p(\Omega)\}$, which, by setting $Q \to \infty$, reduces to

$$B = \begin{cases} B_{\text{plasm}} = \dfrac{1+\varepsilon_\infty}{2}, & \text{(12a)} \\ B_{\text{polar}} = \dfrac{(1+\varepsilon_\infty)^2}{2\varepsilon_\infty}\dfrac{\Omega_{\text{polar}}^2}{\omega_{\text{LO}}^2 - \omega_{\text{TO}}^2}, & \text{(12b)} \end{cases}$$

for Drude and Lorentz materials, respectively.

Equation (8) is the key contribution of this paper. Unlike expressions presented in previous works [41,42], Eq. (8) distinctly separates the role of the optical loss, described by the quality factor Q, in NFRHT, from other dispersion parameters that are captured by B, and temperature. The decoupling of the temperature, material quality factor, and material residue in Eq. (8), via the functions $\Pi(\Omega/T)$ and $\Psi(Q/B)$, allows a quantitative classification of different materials as candidates for tailoring NFRHT.

Equation (8) is a very good approximation of the exact result obtained via fluctuational electrodynamics, for $d \ll \lambda_T$ and Q considerably larger than unity, which is satisfied by all relevant materials for NFRHT [59]. Furthermore, Eq. (8) is *exact* for $\varepsilon_\infty = 1$ in either polar or plasmonic media. We stress that Eq. (11) represents a tight bound to NFRHT that accounts for material dispersion. This is to be contrasted to previous results that derived upper bounds to h with the idealized assumption of a dispersionless perfect blackbody in the near field (i.e., $\xi = 1$) [36], thus yielding a thermal conductance that is orders of magnitude larger than our result in Eq. (8) [see Fig. 4(b) below].

With Eqs. (8) and (10), one can identify the optimal material characteristics, independent of temperature, that maximize NFRHT. In particular, Ψ describes how NFRHT changes with optical loss. Seeking the maximum of Ψ [Eq. (10)], we obtain

$$Q_{\mathrm{opt}} = 4.5B. \tag{13}$$

Hence, NFRHT is maximized when the material quality factor is 4.5 times the material residue function, given in Eqs. (12). The work in Ref. [36] yielded a universal optimal quality factor, namely $Q^*_{\mathrm{opt}} = 2.72$, which, however, is independent of B, thus suggesting that *all* materials that have the same Q should perform identically in terms of NFRHT. In contrast, Eq. (13) demonstrates that other dispersion characteristics, beyond the quality factor, are critical in evaluating the NFRHT response (see Appendix C).

From Eq. (12a), the material residue for plasmonic materials depends only on ε_∞. Typically, $\varepsilon_\infty \lesssim 10$; hence, B_{plasm} remains well below 10. Thus, from Eq. (13), Q_{opt} for plasmonic materials is relatively low, namely $Q_{\mathrm{opt}} \lesssim 50$. Hence, plasmonic materials with good NFRHT performance have high loss (γ) and modest Q, and NFRHT is enhanced due to the broadband nature of the plasmonic resonance. In contrast, the material residue for polar materials, B_{polar} [Eq. (12b)], is inversely proportional to the spectral width of the Reststrahlen band, $(\omega_{\mathrm{LO}} - \omega_{\mathrm{TO}})$. The Reststrahlen band of most polar materials is narrow; hence, $B_{\mathrm{polar}} \gtrsim B_{\mathrm{plasm}}$; therefore, Q_{opt} for polar media is higher than for plasmonic ones. In contrast to plasmonic media, in polar ones, it is the narrowband nature of SPhPs that enhances NFRHT.

In Fig. 2, Eq. (13) is shown with the solid line. We also evaluate the NFRHT performance of several relevant polaritonic emitters considered in the literature. These include polar materials such as silicon carbide (SiC), hexagonal boron nitride (h-BN), and doped semiconductors, e.g., gallium arsenide (GaAs), indium arsenide (InAs) [31,63,64], as well as plasmonic materials such as standard noble metals, e.g., gold (Au), silver (Ag), and heavily doped oxides, e.g., IZO and GZO [31,33,65]. Although the presented framework models NFRHT for materials with only a single polaritonic resonance, i.e., one oscillator in the dielectric permittivity function, in Sec. II D we provide a semianalytical extension able to also describe materials with multiple polaritonic resonances, e.g., SiO_2 [66] or Al_2O_3 [67]. This model is in very good agreement with FE calculations, as long as the polaritonic resonances are spectrally sufficiently distant, as we show for the case of SiO_2.

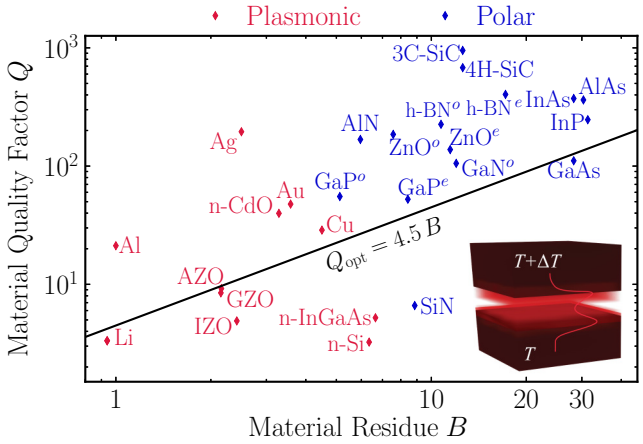

FIG. 2. Material quality factor Q and residue parameter B for plasmonic and polar materials. Drude parameters are taken from Ref. [60] for Au, Ag, Cu, Al. Lorentz parameters for SiN are taken from Ref. [61] (upon fitting), for n-doped Si from Ref. [62], whereas for the rest of the considered materials from Ref. [31]. All doped semiconductors' dispersions are assumed independent from temperature. Superscripts o and e stand for the ordinary and extraordinary principal axes, respectively. The solid line shows Eq. (13), which maximizes NFRHT.

The distance between each point in Fig. 2 and the solid curve representing Eq. (13) expresses how far from the ideal material performance each material falls. Interestingly, an ultrahigh Q does *not* necessarily yield optimal NFRHT. By contrast, it is the interplay between Q and B that is critical, making, for instance, GaAs, AZO, and GaN near-optimal materials for NFRHT as compared to Ag or 3C-SiC, even though the latter exhibit ultrahigh quality factors. This demonstrates the importance of the material residue B in evaluating NFRHT performance.

The parameter h_{max} in Eq. (11) is the maximum radiative thermal conductance achievable for each material, if one adjusted their quality factor such that $\Psi\,(Q/B) \to 1$, and in the limit of infinite temperature, for which $\Pi(\Omega/T) \to 1$. In Fig. 3(a), we calculate h_{max} for the materials considered in Fig. 2. To quantify the degree to which the loss of each material deviates from the optimal value as defined in Eq. (13), we plot these points against the ratio Q/B, which is inversely proportional to γ, the optical loss. Figure 3(a) demonstrates that materials with significantly different quality factors, e.g., Au and Ag, can have similar maximal thermal conductance, if one adjusted their loss. This occurs because the material residue B compensates for the lower

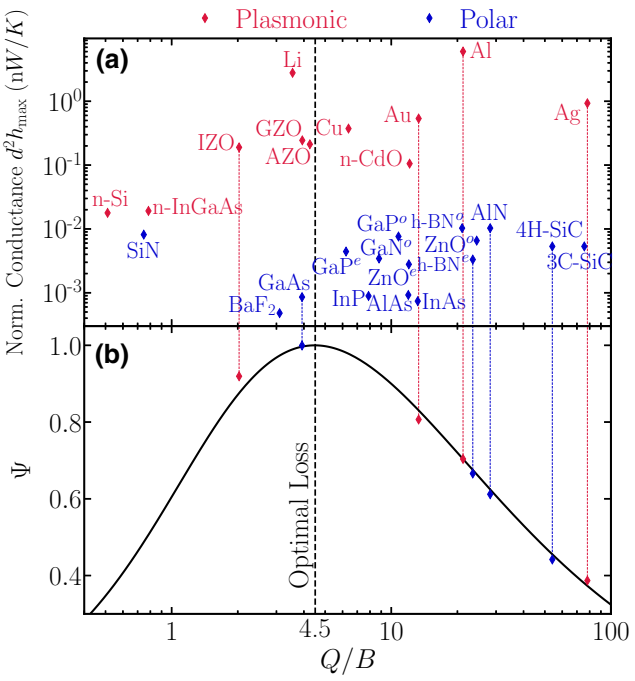

FIG. 3. (a) Maximum heat transfer coefficient $h_{\max}$ [Eq. (11)] for pairs of plasmonic and polar materials as considered in Fig. 2, for optimal loss and infinite temperature. (b) Function Ψ [Eq. (10)] as Q/B varies. The optimal Q_{opt}/B is shown with the dashed vertical line. Points in panel (b) represent fluctuational electrodynamics calculations for the considered materials, and are in very good agreement with our analytical result [Eq. (8)].

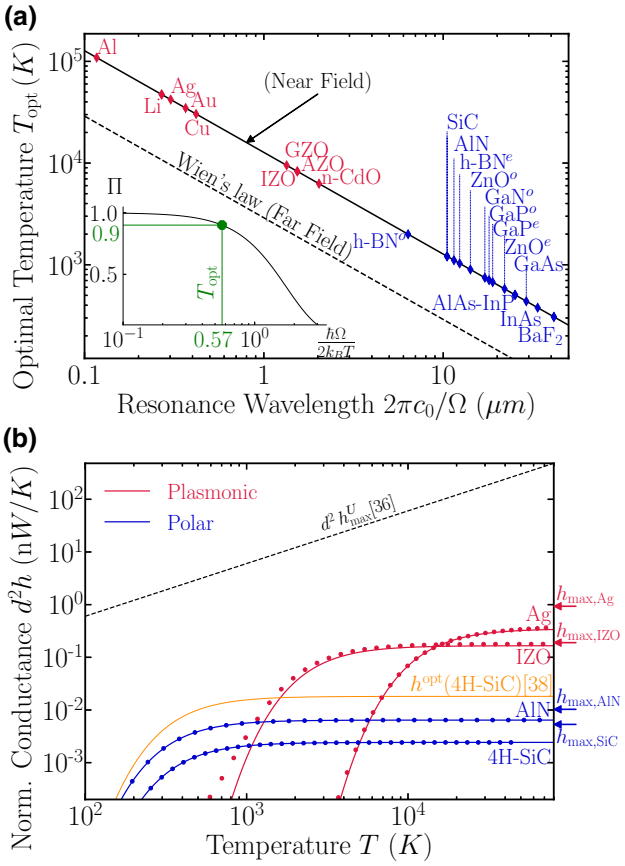

FIG. 4. (a) Optimal temperature T_{opt} as a function of the resonance wavelength, calculated using Eq. (14). The Drude parameters for the Au, Ag, Cu, Al are taken from Ref. [60], while the Drude parameter for the other plasmonic materials and the Lorentz parameters for polar materials are taken from Ref. [31] (Tables 1 and 2). The superscripts o and e stand for the ordinary and extraordinary principal axes of the corresponding material, respectively. In the inset, we plot Π [in Eq. (9)], which expresses the normalized thermal conductance in the optimal loss condition $Q = Q_{\text{opt}} = 4.5B$ [see Eq. (13)]. We identify the optimal operating temperature for a material by setting $\Pi = 0.9$ (green marker). (b) Temperature dependence of the total radiative thermal conductance h [Eq. (8)] for pairs of plasmonic materials (Ag, IZO) and polar ones (AlN, 4H-SiC). Dotted lines show results with fluctuational electrodynamics. The fundamental bound $h^{\text{U}}_{\max} = k_B^2 T/3\hbar d^2$ [36] is shown with the black dashed line and the upper bound h^{opt} by Ref. [38] is shown with the orange curve for 4H-SiC.

Q of Au as compared to that of Ag (see Fig. 2). In other words, small deviations of ε_∞ from unity in plasmonic metals [Eq. (12a)], and, similarly, suboptimal Reststrahlen band spectral widths with respect to Ω in polar materials [Eq. (12b)], can considerably affect the optimal point of NFRHT.

The dependence of NFRHT from the optical loss is captured explicitly in Ψ [Eq. (10)], and is shown graphically in Fig. 3(b). As described in Eq. (13), Ψ is maximum at $Q_{\text{opt}} = 4.5B$, depicted with the vertical dashed line. The horizontal distance between this line and each point in Fig. 3(a) indicates how close each material is to the ideal optical loss, for its particular resonance frequency Ω. For example, despite the comparable material residue B of Ag and Au, the loss (γ) of Au yields a value of Ψ that is much closer to unity as compared to Ag; hence, Au presents overall better NFRHT performance, which is consistent with Fig. 2.

In Fig. 3(b), we also append points that correspond to exact calculations with fluctuational electrodynamics for few commonly used materials in NFRHT. These calculations are performed in the limit of infinite temperature for the sake of a meaningful comparison with our formalism in Eq. (8). It is important to stress that the limit of infinite temperature here has only the mathematical purpose of saturating the function Π, and therefore removing the temperature dependence in h. The exact results, represented as markers, are in very good agreement with our theory (solid line) for all considered materials. Small discrepancies occur in the range of relatively low Q, for example, in the case of IZO [33], since our formalism assumes resonant material response; hence, its accuracy improves as

the material quality factor increases (see Appendix B for details).

C. Temperature dependence

The temperature dependence of NFRHT is described via $\Pi(\Omega/T)$ in Eq. (9), displayed in the inset of Fig. 4(a), which is the only temperature-dependent term in Eq. (8), and agrees with previous analytical results [36,41]. In contrast to Wein's displacement law in the far field, where h scales as T^3, in the near field, Π scales as T^{-2} (for increasing T). On the other hand, from Eq. (11), $h_{\max}$ scales with the resonance frequency; therefore, materials supporting polaritons at high frequencies (high Ω) will, in principle, reach higher NFRHT rates. However, for this to occur in practice, they ought to operate at dramatically higher temperatures. Specifically, since Π decreases exponentially with the ratio Ω/T, to avoid a dramatic damping in h, a higher resonance frequency should be compensated by a higher operating temperature, as expected.

This is well understood in the far-field regime with Wien's displacement law that estimates the optimal resonance frequency of a thermal emitter at a given temperature for maximizing the power emitted in the far field. One can similarly estimate the optimal temperature T_{opt} of a polaritonic thermal emitter in a planar near-field configuration, by maximizing $\Pi(\Omega/T)$. Since Π reaches its maximum $\Pi = 1$ in the limit of infinite temperature, we compute the optimal temperature of operation as a function of the resonance frequency Ω by setting the term $\Pi(\Omega/T)$ to 0.9, as shown with the green lines in the inset of Fig. 4(a). The resulting optimal temperature is expressed as

$$T_{\text{opt}} = \frac{\hbar\Omega}{2k_B 0.57} = \frac{b_{\text{NF}}}{\lambda}, \tag{14}$$

where $b_{\text{NF}} = 12\,729\ \mu\text{m}\,K \approx 4.4 \times b_{\text{Wien}}$ (in which the subscript NF stands for near field) and $\lambda = 2\pi c_0/\Omega$ is the resonance wavelength. This dependence of T_{opt} from Ω is shown with the solid line in Fig. 4(a). As a reference, we also display with the dashed line Wein's displacement law, relevant in the far field. One can therefore see that in the near field considerably higher temperatures are required to reach optimal material performance, as compared to the far field. This is expected, since far-field thermal emission is generally more broadband in comparison to near-field thermal emission, especially for polaritonic materials [43,68]. Hence, the maximal spectral overlap between the mean energy per photon, $\theta(\omega, T)$, and a blackbody spectrum is achieved at much lower temperatures compared to the overlap between a narrowband near-field resonance and $\theta(\omega, T)$, since θ broadens as T increases.

In Fig. 4(a) we also display the optimal temperature, calculated using Eq. (14), as a function of the resonance wavelength $2\pi c_o/\Omega$, for the polar and plasmonic materials considered in Figs. 2 and 3. It can be seen that most polar media, with resonance frequencies mainly in the mid-IR, will achieve optimal performance at temperatures that are up to 2 orders of magnitude lower than their plasmonic counterparts, since plasmonic resonances occur mainly in the near-IR, visible and UV regimes.

This can also be seen in Fig. 4(b), showing the total radiative thermal conductance h computed via our analytical result [Eq. (8)]. We consider a set of plasmonic materials, i.e., IZO and Ag, and a set of polar ones, i.e., 4H-SiC and AlN. It is clear that plasmonic materials reach higher NFRHT than their polar counterparts; however, this occurs at very high temperatures. This is expected since the resonance frequency Ω of plasmonic media is significantly higher than that of polar ones.

In Fig. 4(b), we also append the exact results with fluctuational electrodynamics (dotted lines), where the wave number and frequency integrations are carried out numerically. These are in excellent agreement with our analytical formalism, except for small deviations that occur only for materials with relatively low Q. This is expected, since a low Q suggests a spectrally broadband response, whereas our formalism applies to polaritonic resonances [Fig. 8(a) in Appendix C]. To conclude, for the vast majority of polar and plasmonic materials, one can *exactly* compute their NFRHT properties with Eqs. (8)–(11).

As a reference, in Fig. 4(b), we also show the fundamental limit to the radiative thermal conductance h, i.e., $h^U_{\max} = k_B^2 T/3\hbar d^2$, as derived by Ben-Abdallah *et al.* [36] (dashed line), and the upper bound derived by Venkataram *et al.* [38] for one of the considered materials, viz., 4H-SiC, denoted with h^{opt}(4H-SiC) (orange curve). By comparing with our exact results, both $h^U_{\max}$ and h^{opt}(4H-SiC) represent loose bounds to NFRHT. This is to be contrasted with the expression in Eq. (11), which is the limit to which h actually saturates at high temperatures for optimal loss, i.e., $Q = Q_{\text{opt}}$, for every material [see the right y axis in Fig. 4(b)].

D. Polar dielectrics with multiple polaritonic resonances

Beyond the theory presented in the previous sections, there exist several polaritonic materials, for example SiO_2, Al_2O_3, and MoO_3 that exhibit multiple polaritonic resonances within the IR range [66,67,69]. In this section, we expand upon the results of the previous sections and present a semianalytical method to include multiple polaritonic resonances.

Let us consider the dielectric permittivity $\varepsilon(\omega)$ of the bulk layers as the sum of N Drude or Lorentz oscillators, i.e., $\varepsilon(\omega) = \sum_{n=1}^{N} \varepsilon_n(\omega)$, where the $\varepsilon_n(\omega)$ are given in Eqs. (5). The polaritonic resonance of each oscillator is assumed spectrally far from each other. In this case, a good approximation of the total emission spectrum $\Phi(\omega)$ is given by a superposition of the emission spectra of the

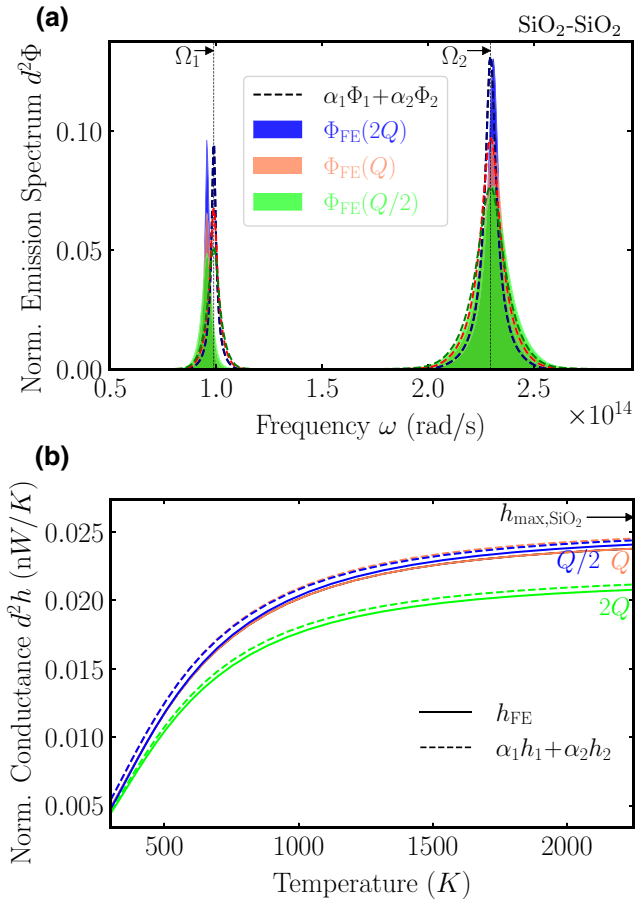

FIG. 5. (a) Thermal emission spectrum Φ normalized with d^2 as a function of frequency for two bulk planar layers of SiO_2 exchanging thermal radiation in the near field. The dispersion relation is the superposition of two Lorentz oscillators, with dispersion parameters $\varepsilon_\infty = 1.007$, $\omega_{TO,1} = 8.6734 \times 10^{13}$ rad/s, $\omega_{TO,2} = 2.0219 \times 10^{14}$ rad/s, $\omega_{LO,1} = 1.0953 \times 10^{14}$ rad/s, $\omega_{LO,2} = 2.5387 \times 10^{14}$ rad/s, $\gamma_1 = 3.3026 \times 10^{12}$ rad/s, $\gamma_2 = 8.3983 \times 10^{12}$ rad/s [66], and resonance frequencies $\Omega_1 = 9.8793 \times 10^{13}$ rad/s and $\Omega_2 = 2.2950 \times 10^{14}$ rad/s. The shaded areas correspond to FE calculations, whereas the dashed lines denote the analytical prediction in Eq. (15) with $\alpha_1 = 0.7, \alpha_2 = 1$. We plot Φ for three values of optical loss, viz., of γ_i, or, equivalently, $Q_i = \Omega_i/\gamma_i$ $(i = 1, 2)$: γ_i (Q_i, in orange), $\gamma_i \to 2\gamma_i$ ($Q_i \to Q_i/2$, in green), $\gamma_i \to \gamma_i/2$ ($Q_i \to 2Q_i$, in blue). In (b), we plot the normalized radiative heat conductance h for the cases considered in panel (a). Solid lines correspond to FE calculations, whereas dashed lines to the analytical prediction in Eq. (16). The total upper bound calculated as $h_{max,SiO_2} = \alpha_1 h_{max,1} + \alpha_2 h_{max,2}$ is also shown.

single oscillators,

$$\Phi(\omega) = \sum_{n=1}^{N} \alpha_n \Phi_n(\omega), \tag{15}$$

where $\Phi_n(\omega)$ is calculated by inserting the single oscillator permittivity $\varepsilon_n(\omega)$ into Eq. (4), and α_n is calculated numerically by fitting $\Phi(\omega)$ with the exact numerical FE result. Assuming that the function $\Pi(\Omega/T)$ is slowly varying with respect to each emission spectrum Φ_n, which peaks at the polariton resonance frequency Ω_n, we can calculate the radiative thermal conductance as the superposition of the single oscillator conductances, i.e.,

$$h = \sum_{n=1}^{N} \alpha_n h_n, \tag{16}$$

where h_n is obtained by plugging each oscillator's parameters, i.e., $\{\Omega_n, Q_n, B_n\}$, into Eq. (8). Therefore, each oscillator has an optimal quality factor $Q_{opt,n} = 4.5B_n$, with the material residue B_n given in Eqs. (12), and an upper bound $h_{max,n}$ given in Eq. (11). The total conductance upper bound h_{max} will be given by the linear combination of each oscillator upper bound, i.e., $h_{max} = \sum_{n=1}^{N} \alpha_n h_{max,n}$.

We apply this approach to describe the radiative heat conductance of two bulk SiO_2 layers, with permittivity given by the sum of two Lorentz oscillators whose parameters, taken from Ref. [66], are given in the figure's caption. By plugging these parameters into Eq. (6b), we calculate the SPhP resonance frequencies, i.e., $\Omega_1 = 9.8793 \times 10^{13}$ rad/s and $\Omega_2 = 2.2950 \times 10^{14}$ rad/s. In Fig. 5(a), we plot the total spectrum Φ_{FE} computed via fluctuational electrodynamics, including s- and p-polarization contributions for $d = 10$ nm, and the spectrum Φ calculated as the sum of the single oscillator contributions. We also calculate the emission spectrum in two other loss scenarios, i.e., $\gamma_i \to 2\gamma_i$ and $\gamma_i \to \gamma_i/2$ $(i = 1, 2)$, corresponding to half or twice the quality factor of the single polariton resonances, respectively, according to the definition in Eq. (7). By setting $\alpha_1 = 0.7$ and $\alpha_2 = 1$, it is evident that there is good agreement between the exact emission spectrum and that reconstructed using Eq. (15) in all considered loss scenarios, with a slight mismatch in the low-frequency resonance contribution, due to the influence of the high-frequency resonance contribution, not taken into account in our model. This agreement is preserved in the corresponding radiative heat conductance h, plotted in Fig. 5(b) as a function of the temperature. The total upper bound h_{max,SiO_2}, calculated as $h_{max,SiO_2} = \alpha_1 h_{max,1} + \alpha_2 h_{max,2}$, is also shown.

III. CONCLUSIONS

We present a simple analytical framework that describes NFRHT in bulk systems with single polaritonic resonance. We derive a universal closed-form expression [Eq. (8)] for the thermal conductance that is valid for most plasmonic or polar materials. This expression clarifies what the roles of the optical loss (γ) and material quality factor ($Q \propto \gamma^{-1}$) are in NFRHT, as well as their interplay with other material

dispersion characteristics. We show that the quality factor of a material's polariton resonance alone is not sufficient to accurately describe NFRHT. In contrast, we introduce the material residue parameter B that completes the analytical framework for the classification of all plasmonic and polar materials for NFRHT.

We derive a material-dependent optimal condition that maximizes NFRHT, namely $Q = 4.5B$, where the quality factor of the polaritonic resonance is inversely proportional to the optical loss, and the material residue is loss independent and encompasses critical properties in polaritonic materials, i.e., the resonance frequency and the spectral width of the Reststrahlen band.

Although previous works have derived upper bounds to the spectral emissivity [38,39,70] and loose upper bounds to the total near-field thermal conductance [16,36], here, we provide a *tight* bound to the thermal conductance, $h_{\max}$. Other than the well-known dependence from the gap size d^{-2}, $h_{\max}$ also rigorously demonstrates the role of other material dispersion characteristics in NFRHT. Finally, we provide a semianalytical extension to our approach, able to describe multiple polaritonic resonances.

ACKNOWLEDGMENTS

This work is dedicated to the memory of John S. Papadakis. The authors acknowledge Dr. Mitradeep Sarkar for creating the schematic drawing in Fig. 2. The authors declare no competing financial interest. G.T.P. acknowledges funding from "la Caixa" Foundation (ID 100010434), from the PID2021-125441OA-I00 project funded by MCIN/AEI/10.13039/501100011033/FEDER, UE, and from the European Union's Horizon 2020 research and innovation programme under the Marie Skłodowska-Curie Grant Agreement No. 847648. The fellowship code is LCF/BQ/PI21/11830019. This work is part of the R&D project CEX2019-000910-S, funded by MCIN/AEI/10.13039/501100011033/, from Fundació Cellex, Fundació Mir-Puig, and from Generalitat de Catalunya through the CERCA program.

APPENDIX A: DERIVATION OF EQ. (4)

We derive the analytical expression of the emission spectrum Φ for two semi-infinite layers made of nonmagnetic, isotropic, homogeneous polaritonic material with relative dielectric permittivity $\varepsilon(\omega)$ and susceptibility $\chi(\omega) = \varepsilon(\omega) - 1$, separated by a vacuum gap of size d.

For gap sizes smaller than the thermal wavelength, evanescent waves ($\beta > k_0$) dominate the heat flux. In this range, the corresponding transmission probability, for p-polarization, can be expressed as [1,2,44,45] $\xi_p(\omega, \beta > k_0) = 4\mathrm{Im}\{r_p\}^2 e^{-2\eta_0 d}/|1 - r_p^2 e^{-2\eta_0 d}|^2$, where $\eta_0 = \sqrt{\beta^2 - k_0^2}$ is the out-of-plane wave number in vacuum, and r_p is the Fresnel coefficient at the vacuum-material interface for p [71]. At sufficiently small vacuum gaps, the dispersion of surface polaritons approaches the quasistatic limit, for which $\beta \gg k_0$ [16]. In this limit, $\eta_0 \approx \beta$, and one can approximate the Fresnel coefficient with $r_p(\omega) = (\varepsilon(\omega) - 1)/(\varepsilon(\omega) + 1)$.

The transmission probability ξ_p for p-polarization in the electrostatic limit $\beta \gg k_0$ can be written as

$$\xi_p(\omega, x) = \frac{4\mathrm{Im}\{r_p(\omega)\}^2 e^{-2x}}{|1 - r_p(\omega)^2 e^{-2x}|^2}. \tag{A1}$$

Perfect photon tunneling occurs at $\xi_p(\omega, \beta) = 1$. From Eq. (A1), this occurs at an in-plane wave number of

$$\beta_{\mathrm{res}}(\omega) = \frac{1}{2d} \ln |r_p(\omega)|^2 = \frac{1}{2d} \ln \left| \frac{\chi(\omega)}{\chi(\omega) + 2} \right|^2. \tag{A2}$$

Equation (A2) is valid for frequencies ω such that $|1 + 2/\chi(\omega)| < 1$, and defines a curve in the (ω, β) parameter space, near which the NFRHT is maximal [36]. The maximum β_{res} that satisfies Eq. (A2) occurs near the surface polariton resonance frequency Ω such that $\mathrm{Re}\{2/\chi(\Omega)\} = -1$ or $\mathrm{Re}\{r_p\} = 0$. At $\omega = \Omega$, Eq. (A2) yields

$$\beta_{\max} \approx \frac{1}{2d} \ln \mathrm{Im}\{r_p\}^2. \tag{A3}$$

The logarithmic dependence of $\beta_{\max}$ from the imaginary part of the Fresnel coefficient showcases the role of material loss in NFRHT [36].

The emission spectrum Φ is therefore given by

$$\begin{aligned} \Phi(\omega) &= \frac{1}{4\pi^2} \int_0^\infty \beta[\xi_p(\omega, \beta) + \xi_s(\omega, \beta)] d\beta \\ &\simeq \frac{1}{4\pi^2} \int_{k_0 d}^\infty \beta \xi_p(\omega, \beta) d\beta \\ &\simeq \frac{1}{4\pi^2} \int_0^\infty \beta \xi_p(\omega, \beta) d\beta \\ &= \frac{1}{4\pi^2 d^2} \int_0^\infty x \xi_p(\omega, x) dx, \end{aligned} \tag{A4}$$

where we have assumed that $k_0 d \ll 1$ and we have made the substitution $\beta d \to x$. By plugging the expression of ξ_p given in Eq. (A1) into Eq. (A4), and by making the substitution $e^{-2x} \to y$, we obtain

$$\begin{aligned} \Phi &= -\frac{\mathrm{Im}\{r_p\}^2}{4\pi^2 d^2} \int_0^1 \frac{\log y}{|1 - r_p^2 y|^2} dy \\ &= -\frac{1}{8\pi^2 d^2} \frac{\mathrm{Im}\{r_p\}}{\mathrm{Re}\{r_p\}} \mathrm{Im}\left\{ \int_0^{r_p^2} \frac{\log y}{1 - y} dy \right. \\ &\quad \left. - \log r_p^2 \int_0^{r_p^2} \frac{1}{1 - y} dy, \right\}. \end{aligned} \tag{A5}$$

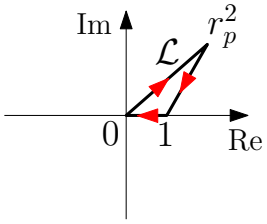

FIG. 6. Contour $\mathcal{L}$ in the complex plane for the identity in Eq. (A6). It is a triangle with vertices $0, 1, r_p^2$, where r_p is the Fresnel coefficient for p-polarization.

We now solve the last two integrals in Eq. (A5). We note that the function $(\log y)/(1-y)$ is analytical inside the contour $\mathcal{L}$ in the complex plane depicted in Fig. 6. Thus, by applying *Cauchy integral's theorem* [72], $\oint_{\mathcal{L}}[(\log y)/(1-y)]dy = 0$; hence, the first integral is solved as

$$\int_0^{r_p^2} \frac{\log y}{1-y}dy = \int_1^{r_p^2} \frac{\log y}{1-y}dy + \int_0^1 \frac{\log y}{1-y}dy = \mathrm{Li}_2[1-r_p^2] - \frac{\pi^2}{6}, \tag{A6}$$

where Li_2 is the dilogarithm or Spence's function, defined as [47]

$$\mathrm{Li}_2(z) = -\int_0^z \frac{\log 1-u}{u}du \quad \text{for all } z \in \mathcal{C}. \tag{A7}$$

The second integral is simply $\int_0^{r_p^2}[(\log r_p^2)/(1-y)]dy = -\log r_p^2 \log(1-r_p^2)$. Therefore, by plugging this result and the one in Eq. (A6) into Eq. (A5), we can express the thermal emission spectrum as

$$\begin{aligned}\Phi &= \frac{1}{8\pi^2 d^2}\frac{\mathrm{Im}\{r_p\}}{\mathrm{Re}\{r_p\}}\mathrm{Im}\left\{-\mathrm{Li}_2[1-r_p^2] + \frac{\pi^2}{6} - \log r_p^2 \log(1-r_p^2)\right\} \\ &= \frac{1}{8\pi^2 d^2}\frac{\mathrm{Im}\{r_p\}}{\mathrm{Re}\{r_p\}}\mathrm{Im}\{\mathrm{Li}_2[r_p^2]\},\end{aligned} \tag{A8}$$

where we have used the dilogarithm identity $\mathrm{Li}_2[z] + \mathrm{Li}_2[1-z] = \pi^2/6 - \log z \log(1-z)$ for all $z \in \mathcal{C} \setminus \{1\}$ [73]. Equation (A8) coincides with Eq. (4) in the main text, and applies to *any* material dispersion. The crucial difference with Ref. [41] is having isolated the term $\mathrm{Re}\{r_p\}$ in the dilogarithm prefactor's denominator, which is central in deriving the simplified final expression for the radiative thermal conductance in Eq. (8).

In the case of the NFRHT between different polaritonic materials with permittivities $\varepsilon_1, \varepsilon_2$, the emission spectrum Φ can be derived as in Eq. (A5), and has the expression

$$\Phi = \frac{1}{4\pi^2 d^2}\left[\frac{\mathrm{Re}\{r_{p,1}\}}{\mathrm{Im}\{r_{p,1}\}} + \frac{\mathrm{Re}\{r_{p,2}\}}{\mathrm{Im}\{r_{p,2}\}}\right]^{-1}\mathrm{Im}\{\mathrm{Li}_2[r_{p,1}r_{p,2}]\}, \tag{A9}$$

where $r_{p,1}, r_{p,2}$ are the Fresnel coefficients at the interfaces with the media of permittivities $\varepsilon_1, \varepsilon_2$, respectively. Equations (A8) and (A9) agree with Ref. [41].

In the low-loss limit, the polariton resonance frequency Ω can be found as the real solution of $\mathrm{Re}\{r_p(\Omega)\} = 0$ [see Eq. (3)]. In this limit, the emission spectrum is maximum at $\omega = \Omega$. As $\lim_{r_p \to 0}\Phi$, we find that (A8) simplifies to

$$\begin{aligned}\Phi_{\max} &= \Phi(\Omega) \\ &= \frac{1}{4\pi^2 d^2}\ln[1 + \mathrm{Im}\{r_p(\Omega)\}^2] \\ &\approx \frac{1}{4\pi^2 d^2}\ln\left[\frac{|\chi|^4}{4\mathrm{Im}\{\chi\}^2}\bigg|_\Omega\right],\end{aligned} \tag{A10}$$

where the identity $\mathrm{Im}\{r_p(\Omega)\} = (|\chi|^2/2\mathrm{Im}\{\chi\})|_{\omega=\Omega}$ was used. Equation (A10) agrees exactly with Eq. (10) of Ref. [37], derived for planar configurations. By contrast, in the high-loss limit, Eq. (3) may have no real solutions, Ω, and the maximum of Φ needs to be calculated by maximizing the right-hand side of Eq. (A8). The range of frequencies for which Eq. (A10) is valid and the threshold between low-loss and high-loss regimes are discussed in the following section.

APPENDIX B: EXACT DERIVATION OF THE RADIATIVE THERMAL CONDUCTANCE

The radiative thermal conductance for two closely spaced semi-infinite layers, given in Eq. (1), can be rewritten as

$$h = \int_0^\infty k_B \Pi\left(\frac{\omega}{T}\right)\Phi(\omega)d\omega, \tag{B1}$$

where Π is given in Eq. (9), and $\Phi(\omega)$ is the emission spectrum, whose closed-form expression has been derived in the previous section and is given in Eq. (A8).

We now particularize this derivation to plasmonic and polar media, whose dispersion relations are given in Eqs. (5a) and (5b), respectively.

We assume that the function $\Pi(\omega/T)$ is slowly varying with respect to the emission spectrum $\Phi(\omega)$, which peaks at the polariton resonance frequency $\bar{\Omega}$. Therefore, we make the first step toward the analytical integration of Eq. (B1) by sampling Π at the frequency $\bar{\Omega}$, i.e., $h = k_B\Pi(\bar{\Omega}/T)\int_0^\infty \Phi(\omega)d\omega$.

We now carry out the frequency integration of the emission spectrum. By using its expression in Eq. (A8), we

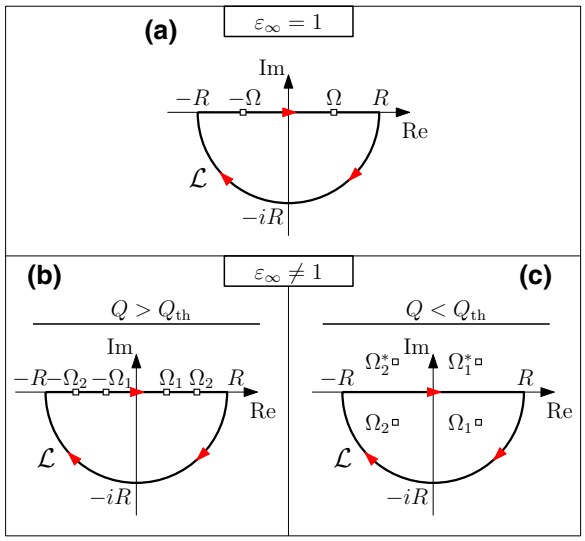

FIG. 7. Contour $\mathcal{L}$ in the complex plane for the complex contour integration in Eq. (B5), composed by the real axis and a semicircular contour of radius R, which will tend to infinity in order to cover the lower half of the complex plane. The poles of the function $f(z)$, defined in Eq. (B4), are shown for the cases $\varepsilon_\infty = 1$ (a), ($\varepsilon_\infty \neq 1, Q > Q_{\rm th}$) (b), and ($\varepsilon_\infty \neq 1, Q < Q_{\rm th}$) (c).

have

$$8\pi^2 d^2 \int_0^\infty \Phi(\omega) d\omega = \int_0^\infty \frac{\mathrm{Im}\{r_p(\omega)\}}{\mathrm{Re}\{r_p(\omega)\}} \mathrm{Im}\{\mathrm{Li}_2[r_p^2(\omega)]\} d\omega. \tag{B2}$$

Since $r_p(\omega)$, inherits the hermiticity (or PT symmetry) from the permittivity function $\varepsilon(\omega)$, i.e., $r_p^*(\omega) = -r_p(-\omega)$ (where the asterisk denotes the complex-conjugate operator), the integrand in Eq. (B2) is an even function of ω. Therefore, we can extend the integration to include the negative frequency axis, namely,

$$8\pi^2 d^2 \int_0^\infty \Phi(\omega) d\omega = \mathrm{Im}\left\{ \int_{-\infty}^{+\infty} f(\omega) d\omega \right\}, \tag{B3}$$

where the complex-valued function $f(z)$ is

$$f(z) = \frac{\mathrm{Im}\{r_p\}(z)}{2\mathrm{Re}\{r_p\}(z)} \mathrm{Li}_2[r_p^2(z)]. \tag{B4}$$

We now tackle the complex integration of $f(\omega)$ in Eq. (B3) by means of contour integration in the complex plane, following a similar strategy to that employed in Ref. [41]. Specifically, we intend to perform the integration on the closed contour $\mathcal{L}$ shown in Fig. 7, comprising the real axis and a semicircular contour of positive radius R lying the lower half-plane, in the limit $R \to \infty$. Since the integrand is vanishing on the semicircular contour in the limit $\lim_{R\to\infty}$, from Jordan's lemma [74], the integral on this contour is also zero. Hence, we can rewrite the integrated emission spectrum as

$$8\pi^2 d^2 \int_0^\infty \Phi(\omega) d\omega = \mathrm{Im}\left\{ \oint_{\mathcal{L}} f(z) dz \right\}. \tag{B5}$$

The function $f(z)$ is the analytical extension of the real-valued function $f(\omega)$ to the complex plane. It must be noted that $\mathrm{Im}\{r_p\}(z), \mathrm{Re}\{r_p\}(z)$ are no longer constrained to be real-valued functions, and therefore the notation $\mathrm{Im}\{\cdot\}, \mathrm{Re}\{\cdot\}$ no longer refers to the real and imaginary operators. Nevertheless, we keep using the same notation in the following calculations for the sake of simplicity, while accounting for the fact that $\mathrm{Im}\{r_p\}(z), \mathrm{Re}\{r_p\}(z)$ are functions derived for the real variable, and extended to the complex plane. For instance, the step $\mathrm{Im}\{r_p(\omega)\} \to \mathrm{Im}\{r_p\}(z)$ for plasmonic dispersions is

$$\begin{aligned} \mathrm{Im}\{r_p(\omega)\} &= \frac{2\varepsilon_\infty \omega \omega_p^2 \gamma}{[(1+\varepsilon_\infty)\omega^2 - \varepsilon_\infty \omega_p^2]^2 + (1+\varepsilon_\infty)^2 \omega^2 \gamma^2} \to \frac{2\varepsilon_\infty z \omega_p^2 \gamma}{[(1+\varepsilon_\infty)z^2 - \varepsilon_\infty \omega_p^2]^2 + (1+\varepsilon_\infty)^2 z^2 \gamma^2} \\ &= \mathrm{Im}\{r_p\}(z), \qquad z \in \mathcal{C}. \end{aligned} \tag{B6}$$

We now carry out the complex integration using Cauchy's residue theorem [74]. The first step is identifying the poles of the integrand $f(z)$. By inspecting the expression of $f(z)$ in Eq. (B4), it is clear that the poles are exactly the frequencies $\bar{\Omega}$ solving the resonance condition in Eq. (3). By solving Eq. (3), using the expressions for the plasmonic and polar permittivities given in Eqs. (5), we have

$$\bar{\Omega}_{\frac{1}{2}} = \Omega, \qquad \varepsilon_\infty = 1, \tag{B7}$$

while

$$\bar{\Omega}_{\frac{1}{2}} = \Omega \sqrt{F - \frac{1}{2Q^2} \mp \frac{1}{2} \sqrt{\left(\frac{1}{Q_{\rm th}^2} - \frac{1}{Q^2}\right)\left(\frac{1}{Q_2^2} - \frac{1}{Q^2}\right)}} \tag{B8}$$

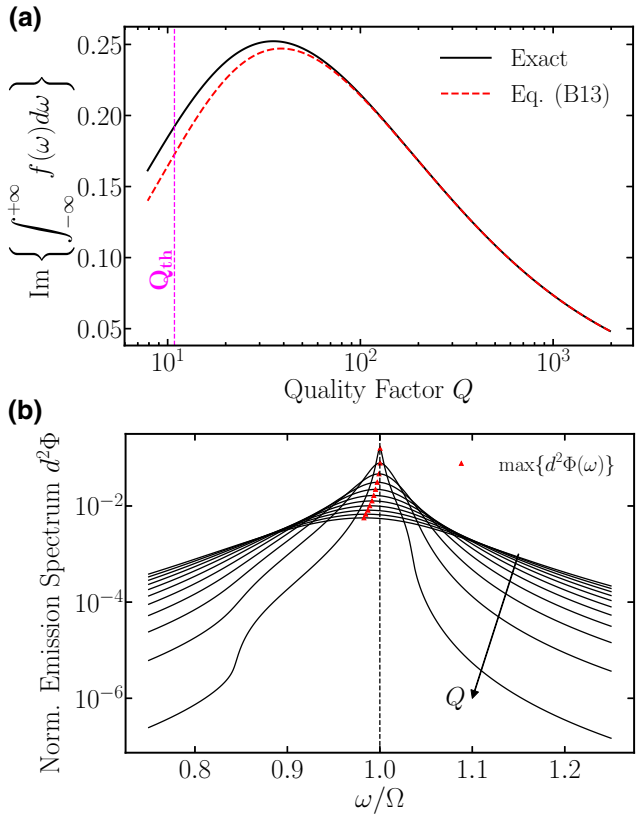

FIG. 8. (a) Integral in Eq. (B5), equivalent to $8\pi^2 d^2 \int_0^\infty \Phi(\omega)d\omega$, for a polar dispersion with Lorentz parameters $\varepsilon_\infty = 4$, $\omega_{\mathrm{TO}} = 1.49 \times 10^{14}$ rad/s, $\omega_{\mathrm{LO}} = 1.83 \times 10^{14}$ rad/s, and resonance frequency $\Omega = 1.77 \times 10^{14}$ rad/s. We compare the exact solution (black curve) calculated using Eq. (B16), with the approximated one (red dashed line) calculated using Eq. (B13), and used as a final result in the main text. We also show with a vertical magenta line the threshold $Q_{\mathrm{th}} = 10.85$ between the low- and high-loss regimes, calculated using Eq. (B10). For the same dispersion parameters, in (b) we plot the emission spectrum normalized by d^{-2} for increasing values of $Q = \Omega/\gamma$, namely, $Q = Q_1/50, Q_1/45, Q_1/40, \ldots, Q_1$, with $Q_1 \approx 200$. We also mark the peak of each emission spectrum with a red marker: in every case, the resonance occurs at frequencies very close to Ω, calculated for $Q \to \infty$.

for $\varepsilon_\infty \neq 1$. Here Ω is the polariton resonance frequency in the absence of optical losses, given in Eqs. (6), and Q is the quality factor of the polaritonic material resonance, defined in Eq. (7). The parameter F for plasmonic and polar cases can be written as

$$F = \begin{cases} F_{\mathrm{plasm}} = 1 + \dfrac{1}{2(B_{\mathrm{plasm}} - 1)}, & \text{(B9a)} \\ F_{\mathrm{polar}} = 1 + \dfrac{\varepsilon_\infty + 1}{2B_{\mathrm{polar}}(\varepsilon_\infty - 1)}. & \text{(B9b)} \end{cases}$$

The parameter B is the material residue function, independent of the material losses (independent of γ), given in Eqs. (12). Finally, the parameters Q_{th} and Q_2 have the expressions

$$Q_{\mathrm{th}} = \frac{1}{\sqrt{2(F - \sqrt{2F-1})}}, \tag{B10}$$

$$Q_2 = \frac{1}{\sqrt{2(F + \sqrt{2F-1})}}, \tag{B11}$$

where the F for plasmonic and polar dispersions are given in Eqs. (B9).

From Eq. (B8), in the case $\varepsilon_\infty \neq 1$, it can be shown that $\bar{\Omega}_{1,2}$ are real numbers only if $Q < Q_2$ and $Q > Q_{\mathrm{th}}$. It can be proven that $Q_2 < 1$, and hence we can focus only on the cases $Q < Q_{\mathrm{th}}$ and $Q > Q_{\mathrm{th}}$. Therefore, Q_{th} represents a threshold for the material quality factor below which the poles of $f(z)$ become complex and move away from the real axis, as shown in Figs. 7(b) and 7(c).

We can now apply the residue theorem to carry out the complex integration in Eq. (B5). It is important to note that, since, for $\varepsilon_\infty \neq 1$ and $Q > Q_{\mathrm{th}}$, the poles of $f(z)$ are on the integration contour, we have to add a $\frac{1}{2}$ factor to the standard residue theorem formula, for which the poles are in the interior of the integration contour $\mathcal{L}$ [74]. On the other hand, the frequency $\bar{\Omega}$ in the case $\varepsilon_\infty = 1$ does not depend on the Q factor, and the poles are always real.

The $\varepsilon_\infty = 1$ case. Via algebraic manipulation, it can be shown that the function $f(z)$ for both plasmonic and polar dispersions in the $\varepsilon_\infty = 1$ case has the expression

$$f(z) = \frac{\Omega}{2Q}\frac{z}{z^2 - \Omega^2}\mathrm{Li}_2[r_p^2(z)]. \tag{B12}$$

Therefore, $f(z)$ has two first-order real poles, i.e., $\{+\Omega, -\Omega\}$, and the integration of Eq. (B5) can be carried out through the residue theorem as

$$\begin{aligned} \mathrm{Im}\left\{\oint_{\mathcal{L}} f(z)dz\right\} &= -\mathrm{Im}\{i\pi[\mathcal{R}\mathrm{es}(f, +\Omega) \\ &\quad + \mathcal{R}\mathrm{es}(f, -\Omega)]\} \\ &= -\mathrm{Re}\{2\pi\mathcal{R}\mathrm{es}(f, +\Omega)\}, \end{aligned} \tag{B13}$$

where $\mathcal{R}\mathrm{es}(f, w)$ is the residue of f at w. Here, we have used the parity of f, and the minus sign comes from having chosen a clockwise (negative) orientation of the contour $\mathcal{L}$, shown in Fig. 7(a).

By taking the limit $\lim_{z\to\Omega}(z - \Omega)f(z)$, we calculate the residue $\mathcal{R}\mathrm{es}(f, +\Omega)$, which has the expression

$$\begin{aligned} \mathcal{R}\mathrm{es}(f, +\Omega) &= \frac{\Omega}{4Q}\mathrm{Li}_2[-\mathrm{Im}\{r_p(\Omega)\}^2] \\ &= \frac{\Omega}{4Q}\mathrm{Li}_2\left[-\left(\frac{Q}{B}\right)^2\right]. \end{aligned} \tag{B14}$$

By plugging this result into Eq. (B13), we can finally write the expression for the radiative thermal conductance as in Eq. (8). It must be noted that all the redundant scaling factors, e.g., B at the denominator of $h_{\max}$ and Ψ, have been introduced such that Ψ would be bounded above by 1.

The $\varepsilon_\infty \neq 1$ case. The function $f(z)$ for both plasmonic and polar dispersions in the $\varepsilon_\infty \neq 1$ case has the expression

$$f(z) = \frac{(F-1)\Omega^3 z}{(z^2-\Omega_1^2)(z^2-\Omega_2^2)} \frac{\mathrm{Li}_2[r_p^2(z)]}{Q}, \tag{B15}$$

where the F are given in Eqs. (B9).

For $\varepsilon_\infty \neq 1$, we have different results according to the position of Q with respect to Q_{th}. From Eq. (B8), it is clear that if $Q > Q_{\mathrm{th}}$ then the function $f(z)$ has four first-order real poles $\{\pm\bar{\Omega}_1, \pm\bar{\Omega}_2\}$, as shown in Fig. 7(b); if $Q < Q_{\mathrm{th}}$ then the function $f(z)$ has four first-order complex poles $\{\pm\bar{\Omega}_1, \pm\bar{\Omega}_2\}$, with $\bar{\Omega}_2 = -\bar{\Omega}_1^*$ as shown in Fig. 7(c). Thus, if $Q < Q_{\mathrm{th}}$, the only poles contributing to the integral are the two in the interior of the contour $\mathcal{L}$, viz., $\{\bar{\Omega}_1, \bar{\Omega}_2\}$. Therefore, in both the $Q > Q_{\mathrm{th}}$ and $Q < Q_{\mathrm{th}}$ cases we can solve Eq. (B5) by applying the residue theorem as follows:

$$\mathrm{Im}\left\{\oint_{\mathcal{L}} f(z)dz\right\} = -\mathrm{Re}\left\{2\pi \sum_{j=1}^{2} \mathcal{R}\mathrm{es}(f, \bar{\Omega}_j)\right\}. \tag{B16}$$

By making the limit $\lim_{z\to\bar{\Omega}_j}(z-\bar{\Omega}_j)f(z)$, we calculate the residues $\mathcal{R}\mathrm{es}(f, \bar{\Omega}_1)$, $\mathcal{R}\mathrm{es}(f, \bar{\Omega}_2)$:

$$\begin{aligned}\mathcal{R}\mathrm{es}(f, \bar{\Omega}_1) &= \mp \frac{F-1}{2\sqrt{4(F^2-1)+1/Q^4-4F(2+1/Q^2)}} \\ &\quad \frac{\mathrm{Li}_2[-\mathrm{Im}\{r_p\}(\bar{\Omega}_1)^2]}{Q}.\end{aligned} \tag{B17}$$

Here the F are given in Eqs. (B9), and the complex function $\mathrm{Im}\{r_p\}(z)$ is the analytical extension of the imaginary part of the Fresnel coefficient in the complex plane [see, e.g., Eq. (B6) for the plasmonic dispersion]. By inserting the residues in Eq. (B17) into Eq. (B16), and in turn plugging this into Eq. (B5), one can finally get the expression for the heat conductance.

APPENDIX C: APPROXIMATIONS LEADING TO EQ. (8)

We now simplify the exact expressions for h, derived in the previous section, for the three scenarios, viz., $\{\varepsilon_\infty = 1 \text{ for all } Q\}$, $\{\varepsilon_\infty \neq 1, Q < Q_{\mathrm{th}}\}$, and $\{\varepsilon_\infty \neq 1, Q > Q_{\mathrm{th}}\}$, aiming at providing a single expression valid in any regime of Q and ε_∞.

We make the following approximations: (i) we neglect the contribution from the second pole $\bar{\Omega}_2$; (ii) we assume that $Q \gg Q_{\mathrm{th}}$. Under these assumptions, we can approximate $\bar{\Omega}_1 \approx \Omega$, with Ω given in Eqs. (6). It can be shown that the resulting residue $\mathcal{R}\mathrm{es}(f, \Omega)$ has the same form as the $\varepsilon_\infty = 1$ case in Eq. (B14), and the heat transfer conductance expression is the same as in Eq. (8).

Even if this expression is derived in the high-Q limit, it also represents a good approximation in the low-Q case, as shown in Fig. 8(a) for a case of study. Specifically, we show the integral in Eq. (B5) for a polar dispersion (see the Lorentz parameters in the figure caption) as a function of the quality factor Q, and there is good agreement with the exact solution over all the considered Q range.

It must be noted that the polariton resonance frequency $\bar{\Omega}_1$ given in Eqs. (B7) and (B8) for both plasmonic and polar dispersions is weakly dependent from the optical loss, i.e., γ or the quality factor Q. In Fig. 8(b) we show this by monitoring the peak position of the emission spectrum $\Phi(\omega)$ for the same polar dispersion used in panel (a), for decreasing values of the quality factor Q or, equivalently, for increasing values of γ, starting from $Q_1 \approx 200$ and reaching $Q = Q_1/50 \approx 4$. It is clear that even in the lowest-Q case the emission spectrum peaks very closely to the resonance frequency Ω calculated in the limit $\gamma \to 0$ or $Q \to \infty$, given in Eqs. (6). Thus, assuming Ω to be the polariton resonance frequency in any material loss condition represents a good approximation.

We now compare the near-field radiative thermal conductance derived in this work with the expression for polar dielectrics provided in Ref. [36]. Ben-Abdallah *et al.* [36] considered a polar material dispersion with high-frequency dielectric permittivity $\varepsilon_\infty = 1$. In their derivation [Eq. (14)], the radiative thermal conductance that they obtained, h', can be written as

$$h' = h'_{\max}\Psi'(Q)\Pi\left(\frac{\Omega}{T}\right), \tag{C1}$$

where $\Pi(\Omega/T)$ is the same as in Eq. (8), given in Eq. (9), and the functions $h'_{\max}$ and Ψ' are given by

$$h'_{\max} = \frac{0.12k_B}{d^2}\Omega, \qquad \Psi'(Q) = \frac{\log Q}{0.37Q}. \tag{C2}$$

In both our result [Eq. (8)] and the result from Ref. [36] [Eq. (C1)], since (Ψ, Ψ') and Π are functions bounded above by 1, $h_{\max}$ and $h'_{\max}$ represent the maximum heat transfer conductances achievable in this configuration. As we showed in the previous sections, the material residue B is greater than unity, i.e., $B > 1$; therefore, we can compare $h_{\max}$ and $h'_{\max}$ as $h'_{\max}/h_{\max} = 4.44B > 4.4$. Therefore, our analytical estimation for the maximum radiative thermal conductance is at least 4.4 times smaller than that predicted in Ref. [36] under the assumption of blackbodylike thermal emission in the near field ($\xi = 1$).

We now compare the functions (Ψ, Ψ'), taking into account the dependence of heat transfer from optical loss.

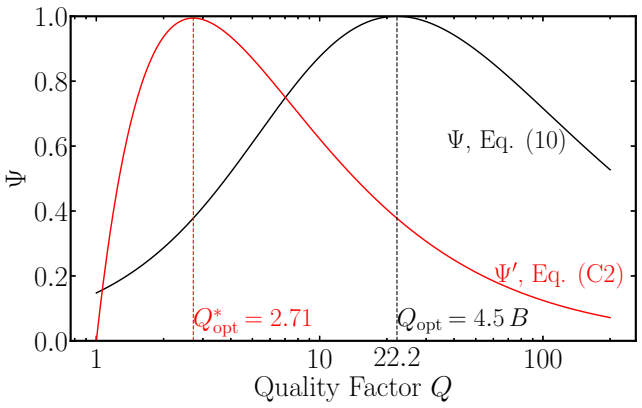

FIG. 9. Functions Ψ (black curve) and Ψ' (red curve), accounting for the optical loss for the NFRHT in a polar bulk system with small vacuum gap, calculated using our result in Eq. (10) and the expression from Ben-Abdallah *et al.* [36] given in Eq. (C2), respectively, as a function of the polariton resonance quality factor Q. We consider a Lorentz dispersion with parameters $\varepsilon_\infty = 1$, $\omega_{\rm TO} = 1.49 \times 10^{14}$ rad/s, $\omega_{\rm LO} = 1.83 \times 10^{14}$ rad/s, for which $B = 4.93$, calculated using Eq. (12b). The different optimal quality factors at which the curves peak are also marked with a dashed line.

The function Ψ' depends only on the quality factor Q of the polariton resonance, and neglects the dependence from the other features of a material's dispersion, such as the size of the Reststrahlen band ($\omega_{\rm LO} - \omega_{\rm TO}$) and its position. In our work, these are included in the material residue B. According to the definition of $\Psi'(Q)$, in Eq. (C2), this function is maximized at the optimal quality factor $Q^*_{\rm opt} = e$, with Napier's constant $e \approx 2.72$, valid for any polar dielectric with a Lorentz dispersion relation [Eqs. (5)], with $\varepsilon_\infty = 1$. Conversely, from our derivation, the function Ψ depends on the dispersion's characteristics through the factor B, and the optimal quality factor Q is given by $Q_{\rm opt} = 4.5\,B$.

In Fig. 9, we compare the two functions for a Lorentz dispersion with $\varepsilon_\infty = 1$, $\omega_{\rm TO} = 1.49 \times 10^{14}$ rad/s, $\omega_{\rm LO} = 1.83 \times 10^{14}$ rad/s, for which $B = 4.93$, calculated using Eq. (12b). The optimal quality factor predicted by maximizing Ψ in Eq. (10) is $Q_{\rm opt} = 4.5B = 22.2$, about an order of magnitude greater than the optimal Q obtained maximizing Ψ' in Eq. (C2).

[1] S. Rytov, Theory of electrical fluctuations and heat emission, Akad. Nauk SSSR **6**, 130 (1953).

[2] D. Polder and M. Hove, Theory of radiative heat transfer between closely spaced bodies, Phys. Rev. B **4**, 3303 (1971).

[3] J. Xu, K. Läuger, R. Möller, K. Dransfeld, and I. H. Wilson, Heat transfer between two metallic surfaces at small distances, J. Appl. Phys. **76**, 7209 (1994).

[4] A. Kittel, W. Müller-Hirsch, J. Parisi, S.-A. Biehs, D. Reddig, and M. Holthaus, Near-Field Heat Transfer in a Scanning Thermal Microscope, Phys. Rev. Lett. **95**, 224301 (2005).

[5] E. Rousseau, A. Siria, G. Jourdan, S. Volz, F. Comin, J. Chevrier, and J.-J. Greffet, Radiative heat transfer at the nanoscale, Nat. Photonics **3**, 514 (2009).

[6] S.-A. Biehs, E. Rousseau, and J.-J. Greffet, Mesoscopic Description of Radiative Heat Transfer at the Nanoscale, Phys. Rev. Lett. **105**, 234301 (2010).

[7] S. Basu, Z. M. Zhang, and C. J. Fu, Review of near-field thermal radiation and its application to energy conversion, Int. J. Energy Res. **33**, 1203 (2009).

[8] G. T. Papadakis, S. Buddhiraju, Z. Zhao, B. Zhao, and S. Fan, Broadening near-field emission for performance enhancement in thermophotovoltaics, Nano Lett. **20**, 1654 (2020).

[9] G. T. Papadakis, M. Orenstein, E. Yablonovitch, and S. Fan, Thermodynamics of Light Management in Near-Field Thermophotovoltaics, Phys. Rev. Appl. **16**, 064063 (2021).

[10] S. Molesky, C. J. Dewalt, and Z. Jacob, High temperature epsilon-near-zero and epsilon-near-pole metamaterial emitters for thermophotovoltaics, Opt. Express **21**, A96 (2013).

[11] B. Zhao, P. Santhanam, K. Chen, S. Buddhiraju, and S. Fan, Near-field thermophotonic systems for low-grade waste-heat recovery, Nano Lett. **18**, 5224 (2018).

[12] M. Francoeur, R. Vaillon, and M. P. Mengüç, Thermal impacts on the performance of nanoscale-gap thermophotovoltaic power generators, IEEE Trans. Energy Convers. **26**, 686 (2011).

[13] J. DeSutter, R. Vaillon, and M. Francoeur, External Luminescence and Photon Recycling in Near-Field Thermophotovoltaics, Phys. Rev. Appl. **8**, 014030 (2017).

[14] N. M. Kerschbaumer, S. Niedermaier, T. Lohmüller, and J. Feldmann, Contactless and spatially structured cooling by directing thermal radiation, Sci. Rep. **11**, 16209 (2021).

[15] R. I. Epstein, M. I. Buchwald, B. C. Edwards, T. R. Gosnell, and C. E. Mungan, Observation of laser-induced fluorescent cooling of a solid, Nature **377**, 500 (1995).

[16] J. B. Pendry, Radiative exchange of heat between nanostructures, J. Phys.: Condens. Matter **11**, 6621 (1999).

[17] S. T. Howell, A. Grushina, F. Holzner, and J. Brugger, Thermal scanning probe lithography—a review, Microsyst. Nanoeng. **6**, 1 (2020).

[18] R. Garcia, A. W. Knoll, and E. Riedo, Advanced scanning probe lithography, Nat. Nanotechnol. **9**, 577 (2014).

[19] H. Hu, H. J. Kim, and S. Somnath, Tip-based nanofabrication for scalable manufacturing, Micromachines **8**, 90 (2017).

[20] H. F. Hamann, Y. C. Martin, and H. K. Wickramasinghe, Thermally assisted recording beyond traditional limits, Appl. Phys. Lett. **84**, 810 (2004).

[21] J. J. M. Ruigrok, R. Coehoorn, S. R. Cumpson, and H. W. Kesteren, Disk recording beyond 100 Gb/in.^{2}: Hybrid recording? (invited), J. Appl. Phys. **87**, 5398 (2000).

[22] M. T. Kief and R. H. Victora, Materials for heat-assisted magnetic recording, MRS Bull. **43**, 87 (2018).

[23] C. R. Otey, W. T. Lau, and S. Fan, Thermal Rectification through Vacuum, Phys. Rev. Lett. **104**, 154301 (2010).

[24] A. Fiorino, D. Thompson, L. Zhu, R. Mittapally, S.-A. Biehs, O. Bezencenet, N. El-Bondry, S. Bansropun, P. Ben-Abdallah, E. Meyhofer, and P. Reddy, A thermal diode based on nanoscale thermal radiation, ACS Nano **12**, 5774 (2018).

[25] P. Ben-Abdallah and S.-A. Biehs, Near-Field Thermal Transistor, Phys. Rev. Lett. **112**, 044301 (2014).

[26] G. T. Papadakis, C. J. Ciccarino, L. Fan, M. Orenstein, P. Narang, and S. Fan, Deep-Subwavelength Thermal Switch via Resonant Coupling in Monolayer Hexagonal Boron Nitride, Phys. Rev. Appl. **15**, 054002 (2021).

[27] C. M. Hargreaves, Anomalous radiative transfer between closely-spaced bodies, Phys. Lett. A **30**, 491 (1969).

[28] G. A. Domoto, R. F. Boehm, and C. L. Tien, Experimental investigation of radiative transfer between metallic surfaces at cryogenic temperatures, J. Heat Transfer **92**, 412 (1970).

[29] J.-P. Mulet, K. Joulain, R. Carminati, and J.-J. Greffet, Enhanced radiative heat transfer at nanometric distances, Microscale Thermophys. Eng. **6**, 209 (2002).

[30] G. T. Papadakis, B. Zhao, S. Buddhiraju, and S. Fan, Gate-tunable near-field heat transfer, ACS Photonics **6**, 709 (2019).

[31] J. D. Caldwell, L. Lindsay, V. Giannini, I. Vurgaftman, T. L. Reinecke, S. A. Maier, and O. J. Glembocki, Low-loss, infrared and terahertz nanophotonics using surface phonon polaritons, Nanophotonics **4**, 44 (2015).

[32] S. A. Maier, *Plasmonics: Fundamentals and Applications* (Springer Science & Business Media, New York, USA, 2007).

[33] J. Kim, G. V. Naik, N. K. Emani, U. Guler, and A. Boltasseva, Plasmonic resonances in nanostructured transparent conducting oxide films, IEEE J. Sel. Top. Quantum Electron. **19**, 4601907 (2013).

[34] X. J. Wang, S. Basu, and Z. M. Zhang, Parametric optimization of dielectric functions for maximizing nanoscale radiative transfer, J. Phys. D **42**, 245403 (2009).

[35] K. Chen, B. Zhao, and S. Fan, MESH: A free electromagnetic solver for far-field and near-field radiative heat transfer for layered periodic structures, Comput. Phys. Commun. **231**, 163 (2018).

[36] P. Ben-Abdallah and K. Joulain, Fundamental limits for noncontact transfers between two bodies, Phys. Rev. B **82**, 121419 (2010).

[37] O. D. Miller, S. G. Johnson, and A. W. Rodriguez, Shape-Independent Limits to Near-Field Radiative Heat Transfer, Phys. Rev. Lett. **115**, 204302 (2015).

[38] P. S. Venkataram, S. Molesky, W. Jin, and A. W. Rodriguez, Fundamental Limits to Radiative Heat Transfer: The Limited Role of Nanostructuring in the Near-Field, Phys. Rev. Lett. **124**, 013904 (2020).

[39] S. Molesky, P. S. Venkataram, W. Jin, and A. W. Rodriguez, Fundamental limits to radiative heat transfer: Theory, Phys. Rev. B **101**, 035408 (2020).

[40] L. Zhang, F. Monticone, and O. D. Miller, in *Frontiers in Optics + Laser Science 2022 (FIO, LS) (2022), paper FW7C.2* (Optica Publishing Group, Rochester, New York, USA, 2022), p. FW7C.2.

[41] E. Rousseau, M. Laroche, and J.-J. Greffet, Asymptotic expressions describing radiative heat transfer between polar materials from the far-field regime to the nanoscale regime, J. Appl. Phys. **111**, 014311 (2012).

[42] H. Iizuka and S. Fan, Analytical treatment of near-field electromagnetic heat transfer at the nanoscale, Phys. Rev. B **92**, 144307 (2015).

[43] B. Song, A. Fiorino, E. Meyhofer, and P. Reddy, Near-field radiative thermal transport: from theory to experiment, AIP Adv. **5**, 053503 (2015).

[44] J. J. Loomis and H. J. Maris, Theory of heat transfer by evanescent electromagnetic waves, Phys. Rev. B **50**, 18517 (1994).

[45] A. V. Shchegrov, K. Joulain, R. Carminati, and J.-J. Greffet, Near-Field Spectral Effects due to Electromagnetic Surface Excitations, Phys. Rev. Lett. **85**, 1548 (2000).

[46] M. Planck, Zur theorie des gesetzes der energieverteilung im normalspectrum, Ann. Phys. **4**, 1 (1901).

[47] L. Lewin, *Dilogarithms and Associated Functions* (Macdonald, London, 1958).

[48] P. Drude, Zur elektronentheorie der metalle, Ann. Phys. **306**, 566 (1900).

[49] A. Kheirandish, N. Sepehri Javan, and H. Mohammadzadeh, Modified Drude model for small gold nanoparticles surface plasmon resonance based on the role of classical confinement, Sci. Rep. **10**, 6517 (2020).

[50] G. Kortüm, in *Reflectance Spectroscopy: Principles, Methods, Applications* (Springer, Berlin, Heidelberg, 1969), p. 103.

[51] M. Francoeur, S. Basu, and S. J. Petersen, Electric and magnetic surface polariton mediated near-field radiative heat transfer between metamaterials made of silicon carbide particles, Opt. Express **19**, 18774 (2011).

[52] X.-J. Hong, T.-B. Wang, D.-J. Zhang, W.-X. Liu, T.-B. Yu, Q.-H. Liao, and N.-H. Liu, The near-field radiative heat transfer between graphene/SiC/hBN multilayer structures, Mater. Res. Express **5**, 075002 (2018).

[53] F. Wang and Y. R. Shen, General Properties of Local Plasmons in Metal Nanostructures, Phys. Rev. Lett. **97**, 206806 (2006).

[54] M. Pascale, S. A. Mann, C. Forestiere, and A. Alù, Bandwidth of singular plasmonic resonators in relation to the Chu limit, ACS Photonics **8**, 3249 (2021).

[55] P.-O. Chapuis, S. Volz, C. Henkel, K. Joulain, and J.-J. Greffet, Effects of spatial dispersion in near-field radiative heat transfer between two parallel metallic surfaces, Phys. Rev. B **77**, 035431 (2008).

[56] K. Esfarjani, G. Chen, and H. T. Stokes, Heat transport in silicon from first-principles calculations, Phys. Rev. B **84**, 085204 (2011).

[57] V. Chiloyan, J. Garg, K. Esfarjani, and G. Chen, Transition from near-field thermal radiation to phonon heat conduction at sub-nanometre gaps, Nat. Commun. **6**, 6755 (2015).

[58] P. S. Venkataram, J. Hermann, A. Tkatchenko, and A. W. Rodriguez, Phonon-Polariton Mediated Thermal Radiation and Heat Transfer among Molecules and Macroscopic Bodies: Nonlocal Electromagnetic Response at Mesoscopic Scales, Phys. Rev. Lett. **121**, 045901 (2018).

[59] As a benchmark, for $Q \gg 1$, considered in Refs. [37,38], the ratio Q/B can be written as $Q/B = |\chi(\Omega)|^2/\mathrm{Im}\{\chi(\Omega)\} = \zeta$, where ζ is a material response factor.

[60] N. W. Ashcroft and N. D. Mermin, *Solid State Physics* (Holt, Rinehart and Winston, New York, 1976).
[61] G. Cataldo, J. A. Beall, H.-M. Cho, B. McAndrew, M. D. Niemack, and E. J. Wollack, Infrared dielectric properties of low-stress silicon nitride, Opt. Lett. **37**, 4200 (2012).
[62] S. Basu, B. J. Lee, and Z. M. Zhang, Infrared radiative properties of heavily doped silicon at room temperature, J. Heat Transfer **132**, 023301 (2009).
[63] M. Cardona and Y. Y. Peter, *Fundamentals of Semiconductors* (Springer, Heidelberg, Germany, 2005), Vol. 619.
[64] M. Schubert, T. E. Tiwald, and C. M. Herzinger, Infrared dielectric anisotropy and phonon modes of sapphire, Phys. Rev. B **61**, 8187 (2000).
[65] H. Kim, M. Osofsky, S. M. Prokes, O. J. Glembocki, and A. Piqué, Optimization of Al-doped ZnO films for low loss plasmonic materials at telecommunication wavelengths, Appl. Phys. Lett. **102**, 171103 (2013).
[66] D.-Z. A. Chen, R. Hamam, M. Soljačić, J. D. Joannopoulos, and G. Chen, Extraordinary optical transmission through subwavelength holes in a polaritonic silicon dioxide film, Appl. Phys. Lett. **90**, 181921 (2007).
[67] K. Z. Rajab, M. Naftaly, E. H. Linfield, J. C. Nino, D. Arenas, D. Tanner, R. Mittra, and M. Lanagan, Broadband dielectric characterization of aluminum oxide (Al_2O_3), J. Microelectron. Electron. Packag. **5**, 2 (2008).
[68] K. Joulain, J.-P. Mulet, F. Marquier, R. Carminati, and J.-J. Greffet, Surface electromagnetic waves thermally excited: Radiative heat transfer, coherence properties and Casimir forces revisited in the near field, Surf. Sci. Rep. **57**, 59 (2005).
[69] W. Ma, P. Alonso-González, S. Li, A. Y. Nikitin, J. Yuan, J. Martín-Sánchez, J. Taboada-Gutiérrez, I. Amenabar, P. Li, S. Vélez, C. Tollan, Z. Dai, Y. Zhang, S. Sriram, K. Kalantar-Zadeh, S.-T. Lee, R. Hillenbrand, and Q. Bao, In-plane anisotropic and ultra-low-loss polaritons in a natural van der Waals crystal, Nature **562**, 557 (2018).
[70] H. Shim, L. Fan, S. G. Johnson, and O. D. Miller, Fundamental Limits to Near-Field Optical Response over Any Bandwidth, Phys. Rev. X **9**, 011043 (2019).
[71] P. Yeh, *Optical Waves in Layered Media* (Wiley, New York, 1988).
[72] J. L. Walsh, The Cauchy-Goursat theorem for rectifiable Jordan curves, Proc. Natl. Acad. Sci. **19**, 540 (1933).
[73] D. Zagier, in *Frontiers in Number Theory, Physics, and Geometry II: On Conformal Field Theories, Discrete Groups and Renormalization* (Springer, Berlin, Heidelberg, 2007), p. 3.
[74] G. F. Carrier, K. Max, and P. Carl E., *Functions of a Complex Variable: Theory and Technique* (Society for Industrial and Applied Mathematics, Philadelphia, Pennsylvania, USA, 2005).

Correction: A byline footnote giving contact information was incorrectly provided for the first author rather than for the second author and has now been rectified.